DJS Vol. 48(2)(2024)- pp.193-205 ISSN: 1012-5965

Delta Journal of Science
Available online at
https://djs.journals.ekb.eg/

Research Article

PHYSICS

Impact of Al^{3+} Substitution on Structural Properties in Nanosized Spinel Copper Ferrites

Alaa Al-radad*, A. A El-Sebaii, Samia A. Saafan, Mohamed M. Elnaggar

Physics Department, Faculty of Science, Tanta University, Tanta 31527, Egypt

***Corresponding author:** Alaa Radad **E-mail:** Alaaabuelyazid@yahoo.com

Received: 24/7/2024 **Accepted:** 25/8/2024

KEY WORDS

Nano Ferrites;

ɛOɣCuAlFe;

ɛOɣCuFe;

XRD;

FTIR

ABSTRACT

Spinel ferrites nanoparticles of the chemical formula $CuAl_xFe_{2-x}O_4$ (where x=0.0, 0.2, 0.4, and 0.6) have been synthesized using the citrate-nitrate auto-combustion technique. The crystal structure's properties of the synthesized nanoparticles have been determined through X-ray diffraction (XRD) and Fourier transform infrared (FTIR) analyses. The extracted XRD data has demonstrated that all samples have a single phase with no undesirable impurities or phases. The samples of (x=0.0 and x=0.2) have a tetragonal structure while the samples of (x=0.4, 0.6) have a cubic spinel structure. The average crystallite size of the nanoparticles is found to be in the accepted nano-size range. The lattice parameter behavior of the tetragonal and cubic samples correlates well with the Jahn-Teller effect and has a trend of increasing with the aluminum addition. Some parameters of crystal imperfections like dislocation density (δ) and strain (ε) have been found to increase with increasing the Al^{3+} concentration and to have an inverse behavior to that of the average crystallite size as expected. Also, the formation of CuAl ferrite samples has been further confirmed by the FTIR spectroscopy where the two prominent absorption bands of ferrites (υ_1 and υ_2) at approximately 592 cm^{-1} and 410 cm^{-1} have been clearly detected.

Introduction

Metallic oxides form an important class of compounds and among them, ferrites are most prominent by virtue of the spinel structure with high thermodynamic stability, low electrical conductivity, electro-catalytic activity, and corrosion resistance (**Deraz**, **2008**). The spinel is a mixed metal oxide with a general formula $M^{2+}M^{3+}{}_2O^{2-}{}_4$ where M is a transition metal ion or a combination of ions (**Beyranvand et al.**, **2022**; **Rahman et al.**, **2022**). Many compounds adopt this type of structure. Moreover, the distribution of cations in magnetic ferrites can be represented by the formula $A[B_2]\ O_4$ where A and B refer to tetrahedral and octahedral sites respectively in the face-centered cubic (FCC) oxygen lattice (**Hussein et al.**, **2023**). There are a total of 56 ions in the unit cell of a spinel, of which 8 are M^{2+} cations, 16 are M^{3+} cations and 32 are O^{2-} anions. Based on the distribution of the divalent and the trivalent metal cations over the A and B-sites, the spinel ferrites are classified into three types: (1) normal spinel, (2) inverse spinel, (3) and mixed spinel. In normal spinel 8 M^{2+} cations are located in A sites and 16 M^{3+} cations are located in B sites, while in inverse spinel 8 M^{3+} cations are located in A sites, and 8 M^{2+} along with 8 M^{2+} cations are located in B sites. In mixed spinels, the cation distribution in the A and B sites is random and different from those of normal and inverse structures. The distribution of cations between tetrahedral (A) and octahedral (B) sites has a significant impact on the crystal structure, as well as the magnetic, electrical, and thermal properties of spinel ferrites. Such feature allows spinels to be used in biomedicine, ecology, electronics, and industry for various applications, including targeted drug delivery (**Pham et al.**, **2020**), magnetic resonance imaging (**Das et al.**, **2021**), battery cathode materials (**Xu et al.**, **2015**), longitudinal recording media (**Arshad et al.**, **2022**), photoanodes (**Kim et al.**, **2020**), and gas sensors (**Pawar et al.**, **2020**).

The attention of researchers has been drawn to the unique spinel copper ferrite because (i) it has a relatively small energy difference between Cu^{2+} ions in the tetrahedral (A) and octahedral (B) sites, cation redistribution is possible and strongly dependent upon the annealing temperature, cooling rate, microstructure, etc. (**Lakhani et al.**, **2010**) (ii) the presence of Cu^{2+} ions can provoke a collective Jahn-Teller distortion which is associated with the alignment of the Cu^{2+} ions occupying the tetragonally distorted octahedral spinel lattice formed by the oxygen ions (**Nedkov et al.**, **2006**) (iii) it has two crystallographic spinel structures, the high-temperature cubic phase (**Almokhtar et al.**, **2004**) and the low-temperature tetragonal phase (**Lakhani et al.**, **2010**).

Researchers previously attempted sporadically to study the effects of doping on the structural, electrical, morphological, photocatalytic, and magneto-dielectric properties of Cu ferrite and they have found

that the substitution of nonmagnetic ions such as Al^{3+} ions in simple and mixed ferrites has received substantial attention over the past few years (**Lakhani et al.**, **2010**) as it can alter the crystal structure, thermal characteristics, and electrical properties of $CuFe_2O_4$ nanoparticles (**Abuilaiwi et al.**, **2022**).

Various techniques have been used to synthesize nanostructured ferrite materials such as sol-gel auto combustion, co-precipitation, high-energy milling, hydrothermal synthesis, and precursor methods. Notably, the sol-gel method has been recognized as environmentally friendly and as having the ability to yield pure, homogeneous nanoparticles. This approach also has facilitated the synthesis of nanoparticles with optimal size and distribution characteristics without using complex equipment or high-cost precursors. The intrinsic qualities of the sol-gel auto-combustion method thus make it an attractive option for researchers aiming to fine-tune nanoparticle characteristics while adhering to sustainable and cost-effective practices (**Badr et al.**, **2024**).

This study represents the characteristics of $CuAl_xFe_{2-x}O_4$ nanoparticles (where x=0.0, 0.2, 0.4 and 0.6), synthesized using the citrate-nitrate auto-combustion technique. It further examines the influence of the Al^{3+} ionic ratio on the structural attributes of the $CuAl_xFe_{2-x}O_4$ nanoparticles. Moreover, the present work paves the way to a future study of the impact of these prepared nanoparticle ferrites on the thermophysical properties - e. g. thermal conductivity, specific heat, and thermal diffusivity - of some phase change materials for thermal energy storage.

Experimental details

Preparation of nanoparticle ferrites

The $CuAl_xFe_{2-x}O_4$ nanoparticles (where x=0.0, 0.2, 0.4, and 0.6) have been prepared by the citrate-nitrate auto-combustion method as per the steps delineated below:

Initially, a combination of chemical reagents including $Cu(NO_3)_2{\cdot}3H_2O$ (≥98% purity, sourced from Loba Chemie), $Fe(NO_3)_3.9H_2O$ (≥98% purity, sourced from Loba Chemie), and $C_6H_8O_7$ (≥99.5% purity, sourced from Loba Chemie) have been adjusted in weights, such that the ratios of the used anhydrous citric acid to trivalent metal ions to divalent metal ions were 3:2:1 (**Banifatemi et al.**, **2021**; **Hussein et al.**, **2021**). The above mentioned nitrate salts have been dissolved in distilled water and stirred for 15 minutes without heating to create a homogeneous mixture before adding the citric acid. Finally, ammonium hydroxide has been added to the mixture in drops with the continuation of the stirring process until the pH reaches approximately 8.0. After removing the magnet, the mixture has been heated for three hours to a temperature of about 120^{o} C. The formed viscous gel has been self-ignited to give eventually a fine and brown powder of the ferrite. The material has been grinded by an agate mortar and sintered at 1000°C for 4 hours. Then a part of the powder has been

pressed into discs and sintered again for density measurements. The other part is left as powder for XRD and FTIR characterization.

The synthesis procedure can be summarized via the following equation:

$Cu(NO_3)_2.3H_2O+(x)Al(NO_3)_3.9H_2O+(2-x)Fe(NO_3)_3.9H_2O+3C_6H_8O_7 \rightarrow CuAl_xFe_{2-x}O_4+$ emitted gasses ↑ → **(1)**

Characterization

The ferrite samples have been characterized using two analytical techniques, including XRD analysis using (PANALYTICAL co. Xpert Pro system in the Central Metallurgical Research and Development Institute in Helwan with a Cu-K_α target and a wavelength of 1.54 Å, 54 kV, and 40 mA), and FTIR spectroscopy using (Bruker Tensor 27 in the Scientific Research Center and Measurements of Tanta University in the range of 350-4000 cm^{-1}).

Results and discussion

XRD analysis

Figure (1) illustrates the XRD patterns of the four prepared samples. For the samples of x=0.0 and x=0.2 respectively, it is revealed the successful preparation of a tetragonal spinel ferrite structure without any detectable impurities in agreement with standard cards of $CuFe_2O_4$ (JCPDS No. 01-072-1174) and (JCPDS No. 01-086-8841). Here it is worth mentioning that many researchers have found that the Cu ferrite sometimes is formed in a tetragonal crystal structure due to Jahn–Teller distortion (**Jiao et al.**, **2013**; **Masunga et al.**, **2021**; **Badr et al.**, **2024**). On the other hand, the pattens of the samples x=0.4 and x=0.6 respectively confirm the successful preparation of a cubic spinel ferrite structure without any detectable impurities in agreement with standard cards of (JCPDS No. 01-089-7408) and (JCPDS No. 01-089-7408).

It is also clearly observed that the diffraction peaks are narrow and sharp, indicating the samples' crystallinity.

Furthermore, the prominent characteristic peaks of the ferrite samples undergo a slight shift mostly towards higher 2θ angles with increasing the aluminum (Al^{3+}) content. This shift is ascribed to d-spacing alteration related to the lattice parameters and the lattice volume. This is attributed to the fact that the Al^{3+} ion has a smaller ionic radius compared to the Fe^{3+} ion (**Ahmad Abuilaiwi et al.**, **2022**). It's also good evidence that aluminum is well-introduced to the copper ferrite.

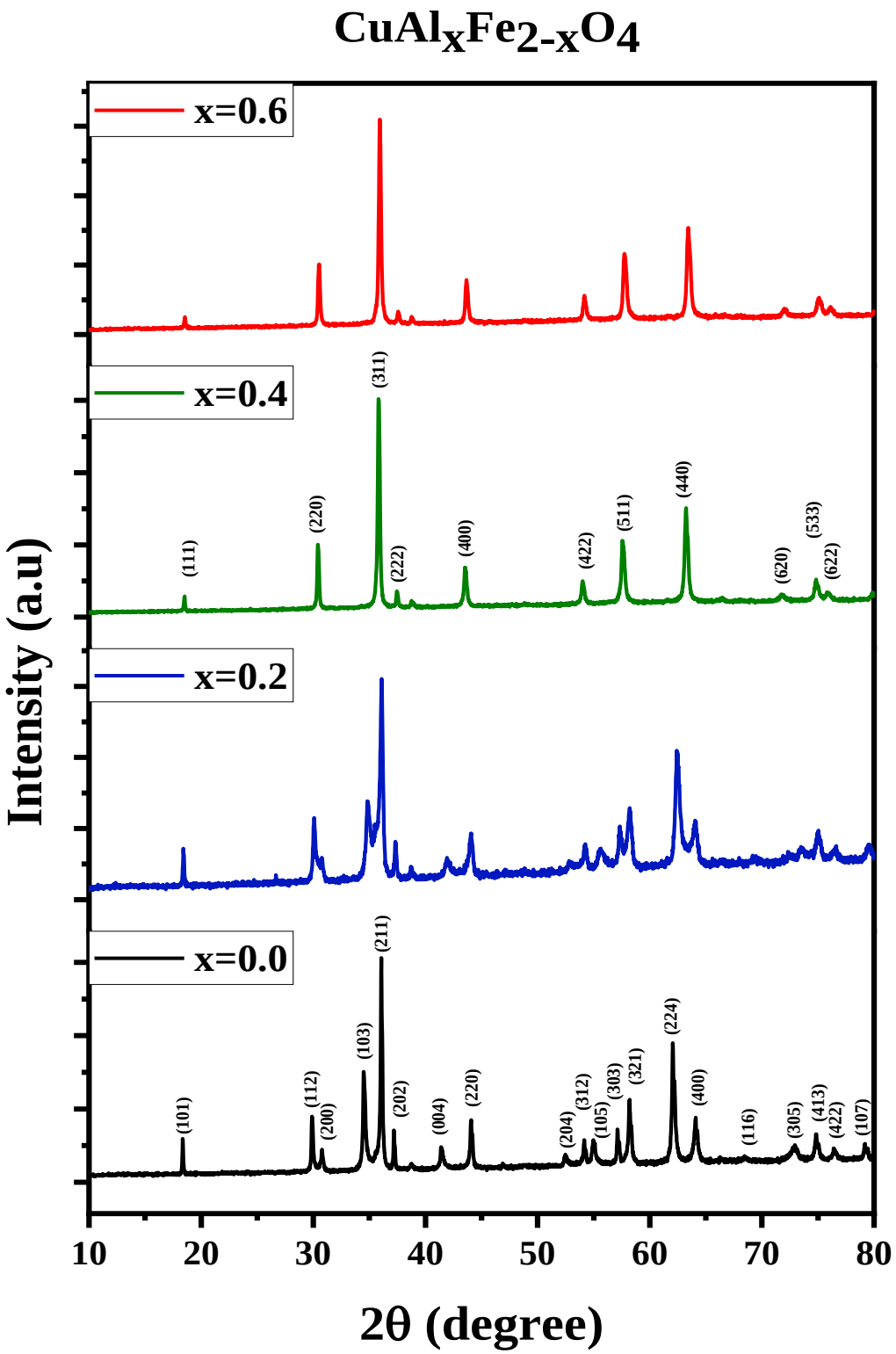

Fig. (1): XRD pattern of $CuAl_xFe_{2-x}O_4$ samples

The average crystallite size has been calculated using Scherrer's formula (**Darwish et al.**, **2023**):

$$R = \frac{k\lambda}{\beta_{1/2}\cos\theta} \rightarrow (2)$$

Where $\beta_{1/2}$ is the full width at half maximum (FWHM) of the main peak representing the plane (211) for the tetragonal structure, and the plane (311) for the cubic structure, θ is Bragg angle, k is the constant dependent on crystallite shape (=0.9 for cubic and tetragonal crystals) and λ is the x-ray wavelength (=1.54 Å).

Lattice constants have been calculated by the following relation (**Mulud et al.**, **2020**):

$$\frac{1}{d_{hkl}^2} = \frac{h^2+k^2}{a^2} + \frac{l^2}{c^2} \rightarrow (3)$$

where d is the interplanar spacing.

Notice that in cubic system a=b=c.

X-Ray density (D_x) of all samples has been calculated too by using (**Darwish et al.**, **2024**) :

$$D_x = \frac{ZM}{N_A Vol} \rightarrow (4)$$

where M is the molecular weight of the sample, N_A is Avogadro's number, Vol is the unit cell volume of the samples ((a^2c) for the tetragonal structure and (a^3) for the cubic structure), and Z varies according to the JCPDS cards of each compound (= 4 for the tetragonal structure and = 8 for the cubic structure).

The samples have been pressed again into discs and the measured density (D_m) of the samples has also been determined by (**Hussein, et al.**, **2023**):

$$D = \frac{m}{Vol} \rightarrow (5)$$

where the sample's mass is donated by m, and Vol is the volume of the sample. Finally, the porosity (P) has been calculated by (**Anjum et al.**, **2020**; **Gayathri Manju et al.**, **2020**) :

$$P = 1 - \frac{D_m}{D_x} \rightarrow (6)$$

Additionally, the following equation can be used to determine the dislocation density, which is denoted by the symbol δ and is described as the quantity of dislocation lines per unit volume of a crystal (**Hussein, et al.**, **2023**):

$$\delta = \frac{1}{R^2} \rightarrow (7)$$

Also, the next formula has been used to calculate the lattice strain (ε) caused by crystal distortions and imperfections in the sample materials (**Salman et al.**, **2016**; **Khan et al.**, **2019**) :

$$\varepsilon = \frac{0.25\,\beta}{\tan\theta} \rightarrow (8)$$

All these results have been listed in Table 1. The average crystallite size, the volume of the unit cell and the porosity of the disc-shaped samples are represented too as functions of x (Al content) in Fig. (2) (a-c).

The crystallite size of the samples ranges from 66.32 nm to 43.47 nm, which is in the accepted nano-size range. It decreases as the aluminum content increases as reported in literature (**Raghavender et al.**, **2012**). This can be attributed to the increase of lattice strain; where an increase in lattice strain is

known to decrease the crystallite size (**Hussein et al., 2023**; **Darwish et al., 2023**). Additionally, the smaller ionic radius of Al^{3+} (54A˚) compared to Fe^{3+} (65 A˚) 22,32,33 [21,30,31] has caused that in the cubic samples as well as in the tetragonal ones, the lattice constant (a) is decreased with increasing the aluminum concentration (x), in agreement with literature (**Raghavender et al., 2012**) Consequently, the unit-cell volume has decreased as expected in both the tetragonal and the cubic structures as the aluminum content increases.

Moreover, according to the XRD data it is well observed that by introducing the aluminum into the formed tetragonal copper lattice, the crystal structure has been turned into a cubic structure overcoming the Jahn-Teller effect (**Almokhtar et al., 2004**; **Badr et al., 2024**)

The X-ray density is a measure of mass per unit volume, while both molecular weight and lattice volume of our samples (for both the tetragonal and cubic structures) decrease with the addition of Al^{3+} ions as the dopant. Hence, the X-ray density (D_x) decreases with increasing the Al^{3+} content as anticipated from equation no. 4. The measured density (D) has the same trend as the X-ray density as it decreases with increasing the aluminum content in both the tetragonal and cubic structures. Also, the X-ray density values (D_x) are higher than the measured density values (D), due to the formation of pores during the pressing and the mentioned above heat treatment (**Kabbur et al., 2018**). However, the porosity has generally small values but showing an increasing trend with increasing the content of Al^{3+} ions in both tetragonal and cubic structures as expected. The calculated parameters of crystal imperfections like dislocation density δ and strain ε increase with increasing the aluminum concentration and have an inverse behavior of the crystallite size as expected.

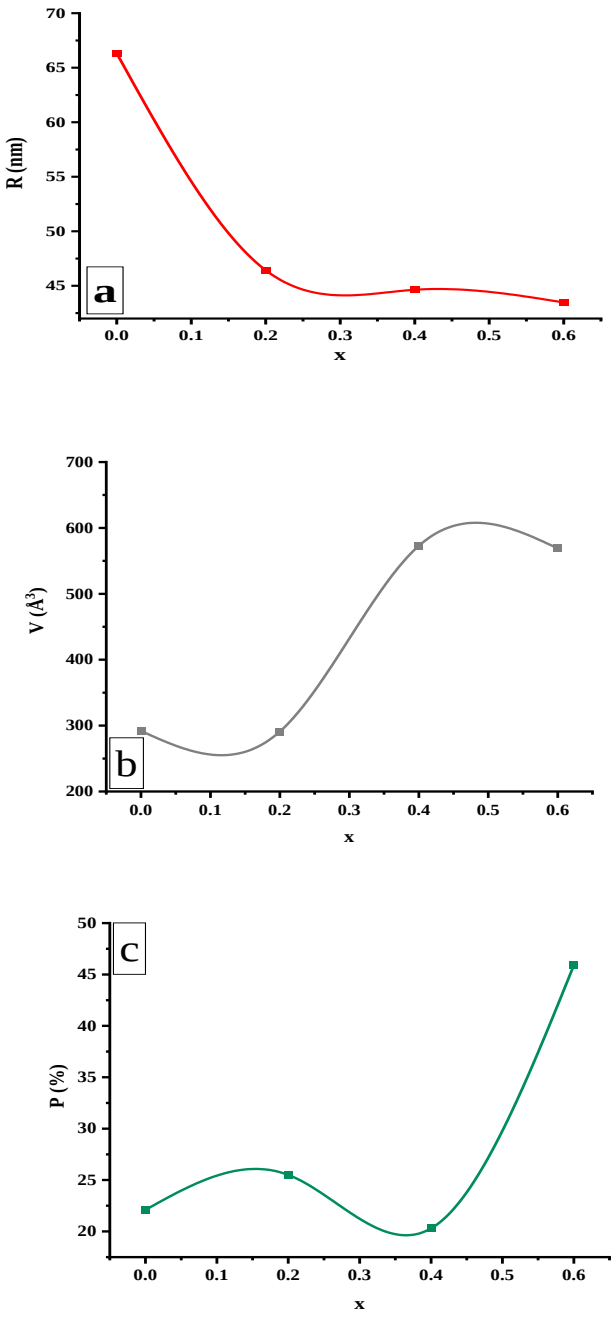

Fig. (2): Crystallite size R (nm), the unit cell volume V (Å^3) and the porosity P of $CuAl_xFe_{2-x}O_4$ (where x=0.0, 0.2, 0.4 and 0.6) as function of Aluminum content (x).

Table (1): The Lattice constant a (Å), average crystallite size R (nm), measured density D (kg/m^3), X-ray density D_x (kg/m^3), Porosity P (%), dislocation density (δ) $^{(m-2)}$, lattice strain (ε), and the unit cell volume V (Å^3) of $CuAl_xFe_{2-x}O_4$ (where x=0.0, 0.2, 0.4 and 0.6)

Sample & method of preparation	a (Å)	Average crystallite size (nm)	D (kg/m^3)	D_x (kg/m^3)	P (%)	Dislocation density (δ) (m^{-2})	The lattice strain (ε)	V (Å^3)
$CuFe_2O_4$ (x=0.0)	a=5.810 c= 8.677	66.32	4207.43	5430.92	22.5	2.27E+14	0.001358	292.58
$CuAl_{0.2}Fe_{1.8}O_4$ (x=0.2)	a=5.809 c= 8.614	46.43	3965.05	5325.80	25.5	4.63E+14	0.001941	291.16
$CuAl_{0.4}Fe_{1.6}O_4$ (x=0.4)	8.308	44.64	4200.59	5273.29	20.3	5.01E+14	0.002497	573.60
$CuAl_{0.6}Fe_{1.4}O_4$ (x=0.6)	8.289	43.47	2796.76	5175.65	45.9	5.28E+14	0.002558	569.61

FTIR of Copper Aluminum Ferrite

Fig. (3) depicts the FTIR spectra of the nanocrystalline $CuAl_xFe_{2-x}O_4$, (where x= 0.0, 0.2, 0.4, and 0.6) ferrite samples measured over the frequency region of 300–4000 cm^{-1}. The obtained FTIR data for the investigated samples is reported in Table (2). Cu-Al ferrites exhibit a distribution of metal cations in two distinct interstitial sites, namely the tetrahedral site (also known as the A-site) and the octahedral site (also known as the B-site) (**Kumar et al.**, **2019**) .

The formation of Cu-Al ferrite samples has been confirmed by two prominent absorption bands (υ_1 and υ_2) at approximately 592 cm^{-1} and 410 cm^{-1} respectively as illustrated in Table (2). The stretching vibrations of tetrahedral metal ions and oxygen bonding [M_{tetra}↔O] are typically associated with υ_1 (**Reyes-Rodríguez et al.**, **2017**) , while υ_2 is commonly associated with the divalent metal ion – oxygen complexes at the octahedral site [M_{octa}↔O] (**Kumar et al.**, **2019**). The values of υ_1 are often higher than the values υ_2 due to the shorter A-site metal-oxygen bonds compared to the B-site metal-oxygen bonds. These two bands are essential features in all FTIR spectra of ferrites documented in the literature.

The absorption bands around 1618 cm^{-1} are related to other O–H (i.e. the sharp peak of hydroxyl group) (or C-H/C-C) groups confirming the existence of interlayer water and the oscillations of the H–O–H bonds (**Darwish et al.**, **2024**). The broad absorption band observed around 3415 cm^{-1} corresponds to O–H bond (i.e. the broad peak of hydroxyl group) stretching vibrations of H_2O present in the interlayer space (**Al Maashani et al.**, **2020**) (**Saafan et al.**, **2021**). Moreover, the small absorption peaks ranged from 2850 to 2920 cm^{-1} may be attributed the carboxyl group.

A small shift of the tetrahedral and octahedral stretching frequency bands (υ_1) and (υ_2) towards the higher frequency region (lower wavenumber region) is observed as illustrated in Table (2) in both the tetragonal and cubic ferrite samples with increasing Al^{3+} content. This shift can be attributed to the bases of reduced mass, bond lengths, and electronegativity of cations (**Nandan et al., 2019**), variation in crystalline size and dispersion of cations (**Rahman et al., 2022**) (**Khan et al., 2021**) at A and B sites.

The force constant of tetrahedral site F_1 and the octahedral site F_2 can be determined using the following equations:

$$F_1 = 4\pi^2c^2\,\upsilon_1^2\mu \rightarrow (9),$$

$$F_2 = 4\pi^2c^2\,\upsilon_2^2\mu \rightarrow (10)$$ (**Hussein et al., 2024**),

where c is the speed of light in vacuum and μ is the reduced mass of the oxygen and metal system, which is equal to 2.061×10^{-23} g.

The collected FTIR data for samples under investigation is tabulated in Table 2. It is noted that the force constant F_1 values are greater than F_2 as anticipated. This can be attributed to the differences in band stretching between υ_1 and υ_2 bands, the stronger cationic interactions at the tetrahedral site, reduced interatomic distance, and higher energy required to break the bonds (**Barde et al., 2022**) . The variation of force constants F_1 and F_2 values is associated with variation in grain size too (**Yadav et al., 2017**).

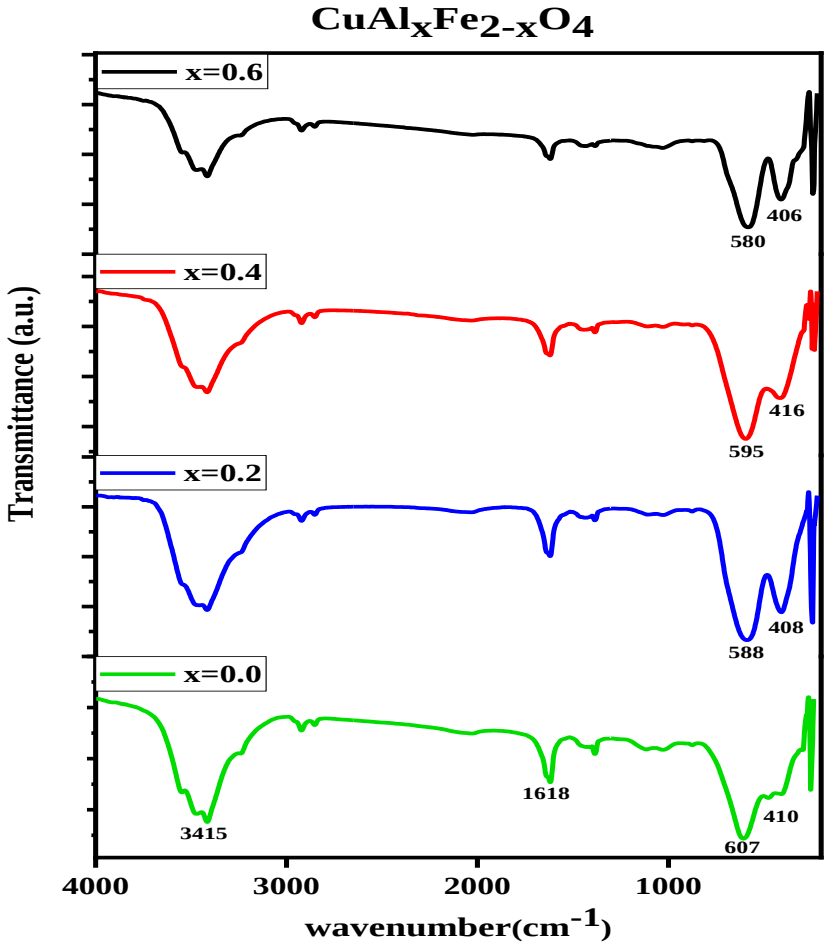

Fig (3): FTIR spectrum of $CuAl_xFe_{2-x}O_4$ samples

Table (2): FTIR absorption band values and force constants, F_1, F_2, at the A- and B-sites, and F_{av} of $CuAl_xFe_{2-x}O_4$ (where x=0.0, 0.2, 0.4 and 0.6)

Sample	υ_1 (cm^{-1})	υ_2 (cm^{-1})	F_1 (dyne/cm)	F_2 (dyne/cm)	F_{av} (dyne/cm)
x=0.0	607	410	269405	122912	196159
x=0.2	588	408	252803	121716	187260
x=0.4	595	416	258858	126536	192697
x=0.6	580	406	245971	120526	183248

Conclusion

$CuAl_xFe_{2-x}O_4$ nanoparticles with (x = 0.0, 0.2, 0.4 and 0.6) have been successfully produced utilizing the citrate-nitrate auto-combustion method. The XRD and FTIR studies illustrate the effect of Al^{3+} doping on the structural properties. The XRD diffraction peaks are narrow and sharp, indicating the samples' crystallinity. The tetragonal structure (samples of x=0.0 and 0.2) has been turned to pure cubic structure (samples of x=0.4 and 0.6) by increasing the Al ion content. The crystallite size (R) has ranged from 66.32 to 43.47 nm, and it has been found to decrease by increasing the aluminum content which correlates well with increasing the lattice strain. Also, the unit-cell volume has decreased in both the tetragonal and the cubic structures as the aluminum content increases in agreement with the lattice parameter behavior. Both the X-ray density and measured density decrease with increasing the Al^{3+} content in both the tetragonal and cubic structures, while the porosities show an increasing trend with the content of Al^{3+} ions in both the tetragonal and the cubic structures. FTIR studies have revealed the presence of the two main absorption bands (υ_1 and υ_2) around 592 cm^{-1} and 410 cm^{-1}. The force constant F_1 values are greater than F_2 values as anticipated.

References

Abuilaiwi A., Faraj, Awais, Muhammad, Qazi, Umair Yaqub, Ali, Farman and Afzal, Adeel (**2022**), Al3+doping Reduces the Electron/Hole Recombination in Photoluminescent Copper Ferrite (CuFe2-XAlxO4) Nanocrystallites. *Bol. la Soc. Esp. Ceram. y Vidr.*, 61(3): 252–262.

Almokhtar, M., Abdalla, Atef M. and Gaffar, M. A. (**2004**), Phase Analysis Study of Copper Ferrite Aluminates by X-Ray Diffraction and Mössbauer Spectroscopy. *J. Magn. Magn. Mater.*, 272–276(III): 2216–2218.

Anjum, Safia, Ilayas, Tafruj and Mustafa, Zeeshan (**2020**), Influence of Antimony Substitution on Structural, Magnetic and Optical Properties of Cadmium Spinel Ferrite. *Appl. Phys. A Mater. Sci. Process.*, 126(3): 1–11.https://doi.org/10.1007/s00339-020-3407-x

Arshad M.I.; Hasan M.S. ; Rehman A.U.; Akht ar M.; Tung D.; Amin N.; Mahmood Kh.; Ali A.; Trakoolwilaiwan Th.; Thanh N.Th. (2022). Structural, optical, electrical, dielectric, molecular vibrational and magnetic properties of La^{3+} doped Mg–Cd–Cu ferrites prepared by Co-precipitation technique. *Ceram. Int.*, 48(10): 14246-14260

Badr, Shimaa, Saafan, Samia A., Soliman, L. I., El-Nimr, M. K., Kamal, Amira A., El-razek Mahmoud, Abd and El-Tahawy, Moustafa (**2024**), Investigation of BaTiO3/ Cu1-XMgxFe_2O_4 Nano-Multiferroic Composites. *J. Magn. Magn. Mater.*, 590.

Banifatemi, S. S., Davar, F., Aghabarari, B., Segura, Juan A., Alonso, Francisco J. and Ghoreishi, Seyyed M. (**2021**), Green Synthesis of CoFe2O4 Nanoparticles Using Olive Leaf Extract and Characterization of Their Magnetic Properties. *Ceram. Int.*, 47(13): 19198–19204.

Barde, N.P., Solanki, P.S., Shah, N.A. and Bardapurkar, P.P. (**2022**), Investigations on Structural, Magnetic, Elastic and Thermodynamic Properties of Lithium Ferrite–Silica Nanocomposites. *J. Mol. Struct.*, 1260: 132771. https://linkinghub.elsevier.com/retrieve/pii/S0022286022004446

Beyranvand, Morteza, Zahedi, Ahmad and Gholizadeh, Ahmad (**2022**), Cadmium Substitution Effect on Microstructure and Magnetic Properties of Mg-Cu-Zn Ferrites. *Front. Mater.*, 8.

Darwish, Moustafa A., Hussein, Marwa M., Omar, Maha K., Abd-Elaziem, Walaa, Yao, Yuan, Klygach, Denis S., Silibin, M. V., Trukhanov, Sergei V., Abmiotka, Nikita V., Tishkevich, Daria I., Zubar, T. I. and Trukhanov, Alex V. (**2024**), Crystal Structure and Peculiarities of Microwave Parameters of Mg1-XZnxFe2O4 Nanospinel Ferrites. *Ceram. Int.*, 50(12): 21027–21039. https://doi.org/10.1016/j.ceramint.2024.03.210

Darwish, Moustafa A., Hussein, Marwa M., Saafan, Samia A., Abd-Elaziem, Walaa, Zhou, Di, Silibin, Maksim V., Trukhanov, Sergei V., Abmiotka, Nikita V., Sayyed, M. I., Tishkevich, Daria I. and Trukhanov, Alex V. (**2023**), Impact of the Mg/Zn Ratio on Features of Structural and Magnetic Properties in A-Site Stoichiometric Nanosized Spinel Ferrites. *J. Alloys Compd.*, 968.

Das, Poushali, Ganguly, Sayan, Margel, Shlomo and Gedanken, Aharon (**2021**), Tailor Made Magnetic Nanolights: Fabrication to Cancer Theranostics Applications. *Nanoscale Adv.*, 3(24): 6762–6796.

Deraz, N. M. (**2008**), Production and Characterization of Pure and Doped Copper Ferrite Nanoparticles. *J. Anal. Appl. Pyrolysis*, 82(2): 212–222.

Gayathri Manju, B. and Raji, P. (**2020**), Green Synthesis, Characterization, and Antibacterial Activity of Lime-Juice-Mediated Copper–Nickel Mixed Ferrite Nanoparticles. *Appl. Phys. A Mater. Sci. Process.*, 126(3): 1–12. https://doi.org/10.1007/s00339-020-3313-2

Hussein, Marwa M., Saafan, Samia A., Abosheiasha, H. F., Zhou, Di, Klygach, D. S., Vakhitov, M. G., Trukhanov, S. V., Trukhanov, A. V., Zubar, T. I., Astapovich, K. A., Zakaly, Hesham M.H. and Darwish, Moustafa A. (**2023**), Crystal Structure and Peculiarities of Microwave Parameters of Co1−xNixFe2O4 Nano Spinel Ferrites. *RSC Adv.*, 13(38): 26879–26891.

Hussein, Marwa M., Saafan, Samia A., Abosheiasha, H. F., Zhou, Di, Silibin, M. V., Trukhanov, S. V., Trukhanov, A. V., Trukhanova, E. L., Astapovich, K. A., Zakaly, Hesham M.H. and Darwish, Moustafa A. (**2023**), Impact of the Ni/Co Ratio on Structural and Magnetic Properties in A-Site Stoichiometric Nanosized Spinel Ferrites. *Ceram. Int.*, 49(23): 39107–39116.

Hussein, Marwa M., Saafan, Samia A., Abosheiasha, Hatem F., Zhou, Di, Tishkevich, Daria I., Abmiotka, Nikita V., Trukhanova, Ekaterina L., Trukhanov, Alex V., Trukhanov, Sergei V., Hossain, M. Khalid and Darwish, Moustafa A. (**2024**), Preparation, Structural, Magnetic, and AC Electrical Properties of Synthesized CoFe2O4 Nanoparticles and Its PVDF Composites. *Mater. Chem. Phys.*, 317(February):129041.https://doi.org/10.1016

/j.matchemphys.2024.129041

Hussein, Marwa M., Saafan, Samia A., Salahuddin, N. A. and Omar, Maha K. (**2021**), Polybenzoxazine/Mg–Zn Nano-Ferrite Composites: Preparation, Identification, and Magnetic Properties. *Appl. Phys. A Mater. Sci. Process.*, 127(7).

Jiao, Hua, Jiao, Gengsheng and Wang, Junlong (**2013**), Preparation and Magnetic Properties of CuFe2O4 Nanoparticles. *Synth. React. Inorganic, Met. Nano-Metal Chem.*, 43(2): 131–134.

Kabbur, S. M., Waghmare, S. D., Ghodake, U. R. and Suryavanshi, S. S. (**2018**), Synthesis, Morphology and Electrical Properties of Co2+ Substituted NiCuZn Ferrites for MLCI Applications. *AIP Conf. Proc.*, 1942: 2–6.

Khan, Mehjabeen, Mishra, Ashutosh, Shukla, Jyoti and Sharma, Pradeep (**2019**), X-Ray Analysis of BaTiO 3 Ceramics by Williamson-Hall and Size Strain Plot Methods. *AIP Conf. Proc.*, 2100(July): 1–6.

Khan, Qaisar, Majeed, Abdul, Ahmad, Nisar, Ahmad, Iftikhar and Ahmad, Rashid (**2021**), Structural Features and Dielectric Behavior of Al Substituted Cu0.7Ni0.3Fe2O4 Ferrites. *Mater. Chem. Phys.*, 273: 125028. https://linkinghub.elsevier.com/retrieve/pii/S0254058421008117

Kim, Jeong Hun, Kim, Hyo Eun, Kim, Jin Hyun and Lee, Jae Sung (**2020**), Ferrites: Emerging Light Absorbers for Solar Water Splitting. *J. Mater. Chem. A*, 8(19): 9447–9482.

Kumar, D. Ravi, Ahmad, Syed Ismail, Lincoln, Ch Abraham and Ravinder, D. (**2019**), Structural, Optical, Room-Temperature and Low-Temperature Magnetic Properties of Mg–Zn Nanoferrite Ceramics. *J. Asian Ceram. Soc.*, 7(1): 53–68. https://doi.org/10.1080/21870764.2018.1563036

Lakhani, V. K. and Modi, K. B. (2010), Al3+-Modified Elastic Properties of Copper Ferrite. *Solid State Sci.*, 12(12): 2134–2143.

Al Maashani, Mohammed S., Khalaf, Kadhim A., Gismelseed, Abbasher M. and Al-Omari, Imaddin A. (**2020**), The Structural and Magnetic Properties of the Nano-CoFe2O4 Ferrite Prepared by Sol-Gel Auto-Combustion Technique. *J. Alloys Compd.*, 817: 152786. https://doi.org/10.1016/j.jallcom.2019.152786

Masunga, Ngonidzashe, Mamba, Bhekie B., Getahun, Yohannes W., El-Gendy, Ahmed A. and Kefeni, Kebede K. (**2021**), Synthesis of Single-Phase Superparamagnetic Copper Ferrite Nanoparticles Using an Optimized Coprecipitation Method. *Mater. Sci. Eng. B*, 272(July): 115368. https://doi.org/10.1016/j.mseb.2021.115368

Mulud, Faten Haithum, Dahham, Najat A. and Waheed, Ibrahim F. (**2020**), Synthesis and Characterization of Copper Ferrite Nanoparticles. *IOP Conf. Ser. Mater. Sci. Eng.*, 928(7).

Nandan, Brajesh, Bhatnagar, M. C. and Kashyap, Subhash C. (**2019**), Cation Distribution in Nanocrystalline Cobalt Substituted Nickel Ferrites: X-Ray Diffraction and Raman Spectroscopic Investigations. *J. Phys. Chem. Solids*, 129: 298–306. https://doi.org/10.1016/j.jpcs.2019.01.017

Nedkov, I., Vandenberghe, R. E., Marinova, Ts, Thailhades, Ph, Merodiiska, T. and Avramova, I. (**2006**), Magnetic Structure and Collective Jahn-Teller Distortions in Nanostructured Particles of CuFe 2 O 4. *Appl. Surf. Sci.*, 253(5): 2589–2596.

Pawar, Hariom, Khan, Meenu, Mitharwal, Chhavi, Dwivedi, U. K., Mitra, Supratim and Rathore, Deepshikha (**2020**), Co1−xBaxFe2O4(X= 0, 0.25, 0.5, 0.75 and 1) Nanoferrites as Gas Sensor towards NO2and NH3gases. *RSC Adv.*, 10(58): 35265–35272.

Pham, Tuyet Nhung, Huy, Tran Quang and Le, Anh Tuan (**2020**), Spinel Ferrite (AFe_2O_4)-

Based Heterostructured Designs for Lithium-Ion Battery, Environmental Monitoring, and Biomedical Applications. *RSC Adv.*, 10(52): 31622–31661.

Raghavender, A. T., Shirsath, Sagar E., Pajic, D., Zadro, K., Milekovic, T., Jadhav, K. M. and Kumar, K. Vijaya (**2012**), Effect of Al Doping on the Cation Distribution in Copper Ferrite Nanoparticles and Their Structural and Magnetic Properties. *J. Korean Phys. Soc.*, 61(4): 568–574.

Rahman, M. M., Hasan, N., Hoque, M. A., Hossen, M. B. and Arifuzzaman, M. (**2022**), Structural, Dielectric, and Electrical Transport Properties of Al3+ Substituted Nanocrystalline Ni-Cu Spinel Ferrites Prepared through the Sol–Gel Route. *Results Phys.*, 38.

Reyes-Rodríguez, Pamela Yajaira, Cortés-Hernández, Dora Alicia, Escobedo-Bocardo, José Concepción, Almanza-Robles, José Manuel, Sánchez-Fuentes, Héctor Javier, Jasso-Terán, Argentina, De León-Prado, Laura Elena, Méndez-Nonell, Juan and Hurtado-López, Gilberto Francisco (**2017**), Structural and Magnetic Properties of Mg-Zn Ferrites (Mg1−xZnxFe2O4) Prepared by Sol-Gel Method. *J. Magn. Magn. Mater.*, 427(June): 268–271.
http://dx.doi.org/10.1016/j.jmmm.2016.10.078

Saafan, Samia A., El-Nimr, Mostafa K., Hussein, Marwa M. and K.Omar, Maha (**2021**), FTIR, DC, and AC Electrical Measurements of Mg Zn Nano-Ferrites and Their Composites with Polybenzoxazine. *Appl. Phys. A Mater. Sci. Process.*, 127(10): 1–14. https://doi.org/10.1007/s00339-021-04947-2

Salman, Sabah A, Hussain, Farouq I and Bakr, Nabeel A (**2016**), Structural Study of Ba 1-x CaxTiO 3 Ceramic Perovskite Material Using X-Ray Diffraction Analysis. *J. Nano. Adv. Mat*, 4(1):

Xu, Gaojie, Liu, Zhihong, Zhang, Chuanjian, Cui, Guanglei and Chen, Liquan (**2015**), Strategies for Improving the Cyclability and Thermo-Stability of LiMn2O4-Based Batteries at Elevated Temperatures. *J. Mater. Chem. A*, 3(8): 4092–4123.

Yadav, Raghvendra Singh, Kuřitka, Ivo, Vilcakova, Jarmila, Havlica, Jaromir, Masilko, Jiri, Kalina, Lukas, Tkacz, Jakub, Švec, Jiří, Enev, Vojtěch and Hajdúchová, Miroslava (**2017**), Impact of Grain Size and Structural Changes on Magnetic, Dielectric, Electrical, Impedance and Modulus Spectroscopic Characteristics of CoFe2O4nanoparticles Synthesized by Honey Mediated Sol-Gel Combustion Method. *Adv. Nat. Sci. Nanosci. Nanotechnol.*, 8(4).

اثر استبدال الالمونيوم الثلاثى على الخصائص الهيكلية في الفريتات النحاسية من النوع السبينل بحجم النانو

الاء أبو اليزيد،احمد السباعى،ساميه سعفان،محمد النجار
جامعه طنطا، كليه العلوم، قسم الفيزياء

تم تصنيع جزيئات الفريتات السبينل بحجم النانو ذات الصيغة الكيميائية $CuAl_xFe_{2-x}O_4$ حيث (x=0,0.2,0.4,0.6) باستخدام تقنية الاحتراق الذاتي بالسترات والنيترات. تم تحديد خصائص التركيب البلوري للجزيئات النانوية المُصنَّعة من خلال تحليل حيود الأشعة السينية (XRD) وتحليل تحويل فورييه للأشعة تحت الحمراء .(FTIR) أظهرت بيانات حيود الأشعة السينية المستخرجة أن جميع العينات تحتوي على طور واحد دون أي شوائب أو أطوار غير مرغوب فيها. تتميز عينات x=0.0) و (x=0.2 بهيكل رباعي السطوح، بينما تتمتع عينات x=0.4) و ٠.٦ (بهيكل مكعب من نوع سبينيل. تم العثور على أن متوسط حجم البلورات النانوية للجزيئات النانوية يقع ضمن النطاق المقبول لحجم النانو. سلوك معامل الشبكة في العينات الرباعية والسداسية يتوافق بشكل جيد مع تأثير جان-تيلر ويظهر اتجاهًا متزايدًا مع إضافة الألمنيوم. تم العثور على أن بعض معاملات عيوب البلورات مثل كثافة الانزلاق (δ)والانفعال (ε) تزداد مع زيادة تركيز Al^{3+} وتظهر سلوكًا عكسيًا مع متوسط الحجم للبلورات كما هو متوقع. كما تم تأكيد تشكيل عينات الفريت النحاس والألمنيوم بشكل إضافي من خلال مطيافية الأشعة تحت الحمراءFTIR ، حيث تم الكشف بوضوح عن نطاقي الامتصاص البارزين للفريتات υ1) و (υ2 عند حوالي ٥٩٢ سم-١ و٤١٠ سم-١.